Advanced Steel Construction – Vol. 21 No. 5 (2025) 413–424
DOI:10.18057/IJASC.2025.21.5.4

STUDY ON THE AXIAL COMPRESSION PERFORMANCE OF CONCRETE FILLED CIRCULAR ALUMINUM ALLOY TUBULAR COLUMN WITH BUILT-IN HOLLOW STEEL TUBE

Zheng-Tao Zhang, Bing Li and Zhou Bo*

School of Civil Engineering, Shenyang Jianzhu University, 25 Hunnan Rd., Liaoning, Shenyang, 110168, China
* *(Corresponding author: E-mail:* wys20020816@163.com*)*

ABSTRACT

In this paper, longitudinal compression tests were conducted on 8 concrete filled aluminum alloy tubular (CFAT) columns with built-in hollow steel tube, and their failure modes, load-strain curve, transverse deformation coefficient, load-displacement curve, axial compressive stiffness and strength coefficient were analyzed. The results show that each component of the specimens have a good deformation coordination. The type of concrete has a notable impact on the bearing capacity and stiffness of member, when the hollow ratio is 0.72, 0.61, and 0.39, the bearing capacity of specimens with ordinary concrete as the sandwich concrete is 43.4%, 37.0%, 39.7% larger than specimens with lightweight concrete as the sandwich concrete, and the axial compression stiffness is 4.8%, 11.3%, and 25% greater than them. The strength coefficients SI of 8 specimens were greater than 1, which indicate a good composite effect between the components. A full-scale finite element model was set up through using ABAQUS software, through numerical simulation, it is found that the load will be mainly borne by the sandwich concrete and aluminum alloy tube, in addition, the analysis of contact stress indicates that there is minimal interaction between the sandwich concrete and the steel tube. To quantify the effects of factors such as the nominal aluminum ratio, compressive strength of the concrete cubes, hollow ratio, and yield strength of the internal tube on axial compressive performance indicators, parametric analyses were conducted. The method suggested for assessing bearing capacity demonstrates good applicability to CFAT column with built-in hollow steel tube.

ARTICLE HISTORY

Received: 16 June 2024
Revised: 8 January 2025
Accepted: 6 February 2025

KEYWORDS

Concrete filled aluminum alloy tubular (CFAT) column;
Built-in hollow steel tube;
Axial compression performance;
Composite effect;
Analysis of the whole stressing process;
Parametric analysis

1. Introduction

The Concrete Filled Double-Skin Steel Tube (CFDST) member represents an innovative structural configuration that entails the substitution of the solid concrete core in a traditional Concrete Filled Steel Tube (CFST) with a hollow steel tube, thereby enhancing the overall structural efficiency and design versatility, The special hollow structure inside not only make the member itself lighter in weight, but also reduce the dosage of concrete, and it has the feature of good ductility, high stiffness, high bearing capacity, and good seismic performance, so it is widely used in piers of viaduct, transmission towers as well as some towering structures or buildings [1-4]. However, in practical engineering applications, due to the influence of external environment, especially in moist environment, the exterior surface of the steel tube is easily corroded owing to long-term contact with moisture in the air, if improper operation and maintenance are not carried out or corresponding measures are not taken in a timely manner, it will have a specific level of detrimental impact on the structure, thereby affecting the service life of the building or structure. Therefore, under the premise of not affecting the mechanical indicators of the member, the selection of materials with strong corrosion resistance to replace external steel tube needs to be given priority consideration.

Aluminum alloy is currently one of the most widely used metal materials, the amount of usage is second only to steel. It was found that its surface has a dense Al_2O_3 protective layer by tracing its chemical essence, which can effectively block the further reaction between air and internal aluminum, therefore, its corrosion resistance is strong, meanwhile, its weight is relatively light. With the support of the above advantages, it ultimately became the preferred choice among numerous corrosion-resistant materials. This composite component composed of aluminum alloy pipes, concrete, and steel is called CFAT member with built-in hollow steel tube. Due to the good corrosion resistance and small self-weight of aluminum alloy, they not only meet the durability performance of the structure or components, but also satisfy the demands of lightweight design of the structure, meanwhile, the application of aluminum alloy materials greatly reduces the incremental costs caused by frequent replacement of accessories, while also reducing the consumption of steel.

Researchers in the relevant discipline have undertaken exhaustive research on the behavior under single or multiple load conditions and the design principle of aluminum-concrete composite structural systems. Zeng et al[5] examined the mechanical characteristics of aluminum alloy tube-encased concrete short columns subjected to axial compression， their findings indicate that the aluminum alloy tube and concrete interact synergistically throughout the stress process, and the proposed method for calculating bearing capacity provides a reasonable estimation of the specimen's relevant mechanical properties. Li et al [6] utilized finite element simulations to analyze the axial compression mechanical properties of 7075 high-strength aluminum alloy tubular concrete columns, and introduced a practical calculation method for bearing capacity based on pertinent steel tube structural specifications. Chen et al. [7] performed axial compression tests on 16 seawater sea-sand concrete-filled aluminum alloy circular tubular columns, exploring their compressive working mechanism and synergistic behavior. Additionally, references [8-13] offer detailed analyses of the related properties of aluminum alloy tube-concrete composite members, with the resulting research contributions serving as valuable references for future studies.

Nowadays, the Investigations into the axial compression mechanical properties of CFAT columns has been relatively mature, however, there have been no reports on the research of CFAT with built-in hollow steel tube proposed in this article, therefore, this paper designed a total of 8 specimens for axial compression testing research, analyzed the failure modes of specimens, and further studied the mechanical performance indicators such as load-strain curve, load-displacement curve, stiffness, and bearing capacity. Due to constrained by test conditions and number of specimens, this paper conducted finite element simulation calculations on the basis of experimental research, analyzed the working mechanism of the specimens, include analysis of the whole stressing process and contact stress analysis. Furthermore, the influence of diverse parameters, including nominal aluminum ratio, concrete cube compressive strength, hollow ratio, and yield strength of internal steel tube on the bearing capacity, axial compressive stiffness, and ductility of specimens has been investigated. Eventually, a streamlined approach for assessing bearing capacity was suggested based upon relevant technical regulations and parameter analysis.

2. Basic situation of the experiment

2.1. Design and processing of specimens

Before the experiment is conducted, a total of 8 CFAT column with built-in hollow steel tube were designed. The components that make up the specimen are aluminum alloy tube, sandwich concrete, and steel tube from the outside to the inside in sequence, In the diagram presented in Fig.1. All specimens have been designed with a height of 720mm. (H=720mm), the cross-sectional diameter is 240mm (D_o=240mm), and the wall thickness of aluminum alloy tube is 5.5mm (t_o=5.5mm). The experimental parameters include hollow ratio χ , the wall thickness t_i of internal steel tube , and concrete type. Table1 provides a comprehensive overview of the parameter specifications and significant outcomes obtained from the conducted tests.

Depending on the type of sandwich concrete, two series of specimens were designed in this test，they are respectively the HACSC series with ordinary concrete as sandwich concrete and the HALCSC series with lightweight concrete as sandwich concrete. The processing steps of the specimen need to be implemented in the following sequence: (1) Placing the rolled steel tube on the

bottom end plate and continuously adjusting its position until the centerline of the steel tube aligns with the centroid of the bottom end plate, and ensuring that the steel tube is perpendicular to the bottom end plate, then, welding the steel tube and bottom end plate together. (2) Concentrically place the aluminum alloy tube on the outside of the steel tube, and angle steel and self-tapping nails are used to achieve the effective connection between the aluminum alloy tube and bottom end plate, the connection form is shown in Fig.2(a). (3) The concrete is poured into sandwich area of aluminum alloy tube and steel tube by using a layered pouring method and vibrates continuously to guarantee the compactness of concrete (In order to prevent concrete from shrinkage due to chemical reactions during the curing stage, the final batch of poured concrete is slightly higher), subsequently, it is cured for 28 days under specific conditions. (4) The excess slurry accumulated on the top of the specimen is chiseled to achieve a level surface that aligns with the aluminum alloy tube and steel tube, then polish the specimen's surface. The polished specimen is depicted in Fig.2(b).

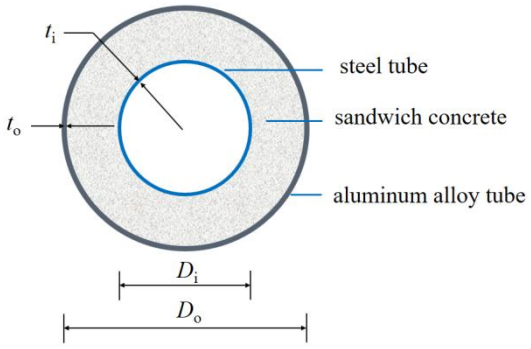

Fig. 1 Internal cavity structure of the specimen and detailed schematic of each part

Table 1
Specimen parameter information and test results (finite element results)

Specimen number	D_0/mm	t_0/mm	D_i/mm	t_i/mm	H/mm	χ	Concrete type	Test and finite element calculation results		
								$N_{ue\,test}$（kN）	$N_{ue\,FEM}$(kN)	*Nue FEM/Nue test*
HACSC1-1	240	5.5	165	4	720	0.72	Ordinary concrete	2782.6	2693.7	0.97
HACSC2-1	240	5.5	140	4	720	0.61	Ordinary concrete	2863.2	2775.6	0.97
HACSC3-1	240	5.5	89	4	720	0.39	Ordinary concrete	3115.2	3066.6	0.98
HACSC3-2	240	5.5	89	3	720	0.39	Ordinary concrete	3023.2	3001.4	0.99
HALCSC1-1	240	5.5	165	4	720	0.72	Lightweight concrete	1939.8	2039	1.05
HALCSC2-1	240	5.5	140	4	720	0.61	Lightweight concrete	2089.6	2121.4	1.02
HALCSC3-1	240	5.5	89	4	720	0.39	Lightweight concrete	2229.9	2214.6	0.99
HALCSC3-2	240	5.5	89	3	720	0.39	Lightweight concrete	2184.2	2132.9	0.98
Average value										0.99
Standard deviation										0.04

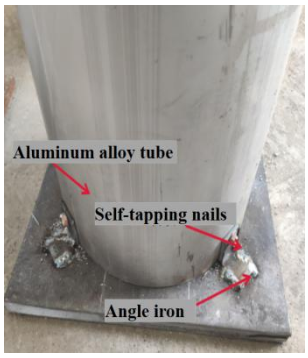

(a) Connection between aluminum alloy and end plate

(b) Polished specimens

Fig. 2 Sketch map of the key processes during specimen processing

2.2. Properties of materials

2.2.1. The aluminum alloy

The aluminum alloy tube type for making the specimens is 6061-T6. Pursuant to the Chinese standard GB/T 228.1-2010 regulation，the tensile coupon tests will be implemented, 4 tensile coupons are cut from the raw materials used to make the specimen. Within a period of time after starting the tensile test, there is no change in the appearance of the tensile coupon, As the force applied by the tensile testing machine gradually increases, when the tensile force reaches a certain value, the middle of the tensile coupon suddenly fractures without any signs, and the elongation is small. From the failure of the specimen, it can be seen that the fracture section is perpendicular to the length direction of the coupon, and the size of the fracture section remains almost unchanged. After the experiment is completed, the data collected from 4 sets of samples will be processed, the relevant mechanical properties indicators of aluminum alloy tube are shown in Table 2, which involves nominal yield strength (the point of conditional yield at which residual strain reaches 0.2%), ultimate strength, elastic modulus and Poisson's ratio.

Table 2
Mechanical property index of aluminum alloy tube

Material type	Nominal yield strength/MPa	Ultimate strength/MPa	Elastic modulus/MPa	Poisson's ratio
Aluminum alloy	210.9	252	69645	0.35

2.2.2. Sandwich concrete

Two types of sandwich concrete were used during the specimen fabrication process, which includes ordinary concrete and lightweight concrete, the mixture proportions of the above two types of sandwich concrete are shown in Table 3. Based on the guidance of the Chinese standard GB/T50081-2019, the real strength of the above two types of concrete has been determined, common concrete and lightweight concrete is 43.8Mpa and 22.1Mpa respectively

Table 3
Mixture proportions of different types of sandwich concrete

The type of concrete	cement	sand	fly ash	Cobble	large particle ceramsite	Medium size ceramic particles	Small particle ceramsite	tail mineral fly-ash	Water reducer	water
Ordinary concrete	284	795	72	1124	--	--	--	--	5	150
Lightweight concrete	486	389	--	--	83	122	122	85	5.8	170

2.2.3. Steel tube

The steel type with built-in steel tube is Q235B. Based on the Chinese standard GB/T 228.1-2010 regulation [14], the mechanical properties of steel tube are obtained by pull-out Test, the tensile coupon are taken from steel tubes of different sizes, the mechanical properties indicators pertaining to steel tubes of differing sizes are detailed in Table 4, f_y and f_u represent the yield strength and ultimate strength of steel tube respectively in Table 4.

Table 4
Mechanical properties indicators of steel tube

Material	f_y/MPa	f_u/MPa	Poisson's ratio
Steel plate (t_i=4mm)	327.7	460.3	0.297
Steel plate (t_i=3mm)	321.4	440.5	0.301

2.3. Test preparation

2.3.1. Layout of data collection points

To analyze the deformation law of the aluminum alloy tube, strain gauges were positioned in the midsection of aluminum alloy tube, both transverse and longitudinal. The setup of the gauges is portrayed in Fig.3(a) and (b), where AL1-L ～ AL4-L denote the longitudinal gauges, and AL1-T ～ AL4-T represent the transverse gauges affixed to the exterior of the aluminum alloy tube.

2.3.2. Experimental loading scheme and loading system

The experiment was executed in the structural laboratory of Liaoning provincial transportation planning and design institute, 500T hydraulic testing machine was used for graded loading. Four displacement gauges are arranged perpendicular to specimen to measure the transverse displacement, which are arranged in a ring with an interval angle of 90 °, and the longitudinal displacement is measured by two displacement gauges arranged on the diagonal of the loading plate. Pre-loading is recommended to be done before formal loading to ensure good contact between the components of the specimens and the normal operation of the machine. In this experiment, the load value of pre-loading was approximately 10% of the estimated ultimate bearing capacity (The result of Numerical simulation calculation), after verifying that there were no other issues, the pre-loading was unloaded and then formally loaded. During the formal loading stage, a graded loading system was implemented, incrementally applying a load that is roughly 10% of the estimate ultimate load-bearing capacity at each stage, and the load of each level was sustained for a period of 2 to 3 minutes.

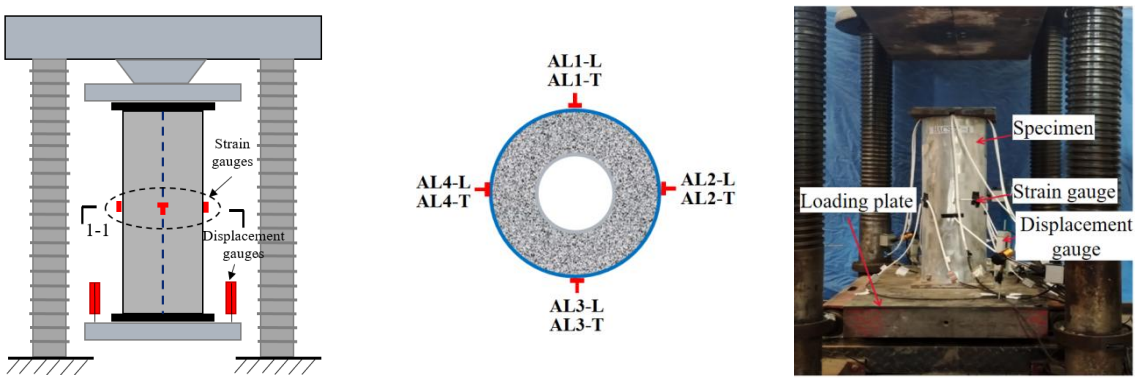

(a) Schematic diagram of the test device (b) Strain gauge placement (b) the test device

Fig. 3 Measurement point arrangement and test loading device

3. Analysis of experiment results

3.1. Failure mode of the specimen

Axial compression tests were conducted on 8 CFAT columns with built-in hollow steel tube. Through observation, it was found that the test phenomena and final failure modes of the 8 specimens from the beginning of loading to the end of the test were basically similar. This paper introduces two specimens numbered HACSC1-1 and HALCSC1-1 as examples.

During the inception phase of the loading, because of the small load, all components of the specimen are in a uniaxial compression state, and the specimen will make a slight sound under axial compression, and the specimen's exterior exhibits no apparent alterations; As the load progressively rises, reaching approximately $0.7N_{ue}$, the specimen produces audible cracking sounds, aluminum alloy tube begin to occur local bulging phenomenon, which is mostly appears near the height of H/2, the root cause for this destructive phenomenon primarily hinge on two aspects, on the one hand, under axial compressive loading, the middle section of the member typically bears the maximum compressive stress, due to the effect of stress concentration, the aluminum alloy tube and concrete in this area are more prone to deformation. On the other hand, when the concrete is compressed, the aluminum alloy tube provides lateral confinement to prevent lateral expansion of the concrete. However, when the compressive stress exceeds a certain limit, the lateral deformation of the concrete increases, leading to buckling of the aluminum alloy tube; As the load increases from $0.7N_{ue}$ to N_{ue}, the outward deformation of the aluminum alloy tube becomes more noticeable, with the concrete at the deformed position being crushed simultaneously; The load gradually decreases after exceeding the ultimate bearing capacity N_{ue}, however, the axial deformation and section transversal deformation of the specimen continue to increase, eventually, the aluminum alloy at H/2 height is torn, which marks the complete destruction of the specimen, the final destruction phenomenon is shown in Fig. 5 (a). For the purpose of further observing the failure mode of the sandwich concrete and the internal steel pipe, the specimen is dissected, it is found that the concrete corresponding to the bulging position of the aluminum alloy tube is crushed, and the inner wall of steel tube in the corresponding position will also be sunken inward.

Moreover, an assessment was performed on the failure behavior of specimen HALCSC1-1, with Fig.5(c) and 5(d) illustrating the failure mode of the specimen and its constituent component. Upon close examination, it was determined that the failure modes of specimens HACSC1-1 and HALCSC1-1 showed a high degree of consistency. The experimental phenomena of specimen HACSC1-1 and HALCSC1-1 show that aluminum alloy tube and sandwich concrete have a good deformation coordination under axial compression, which exhibit a good composite effect.

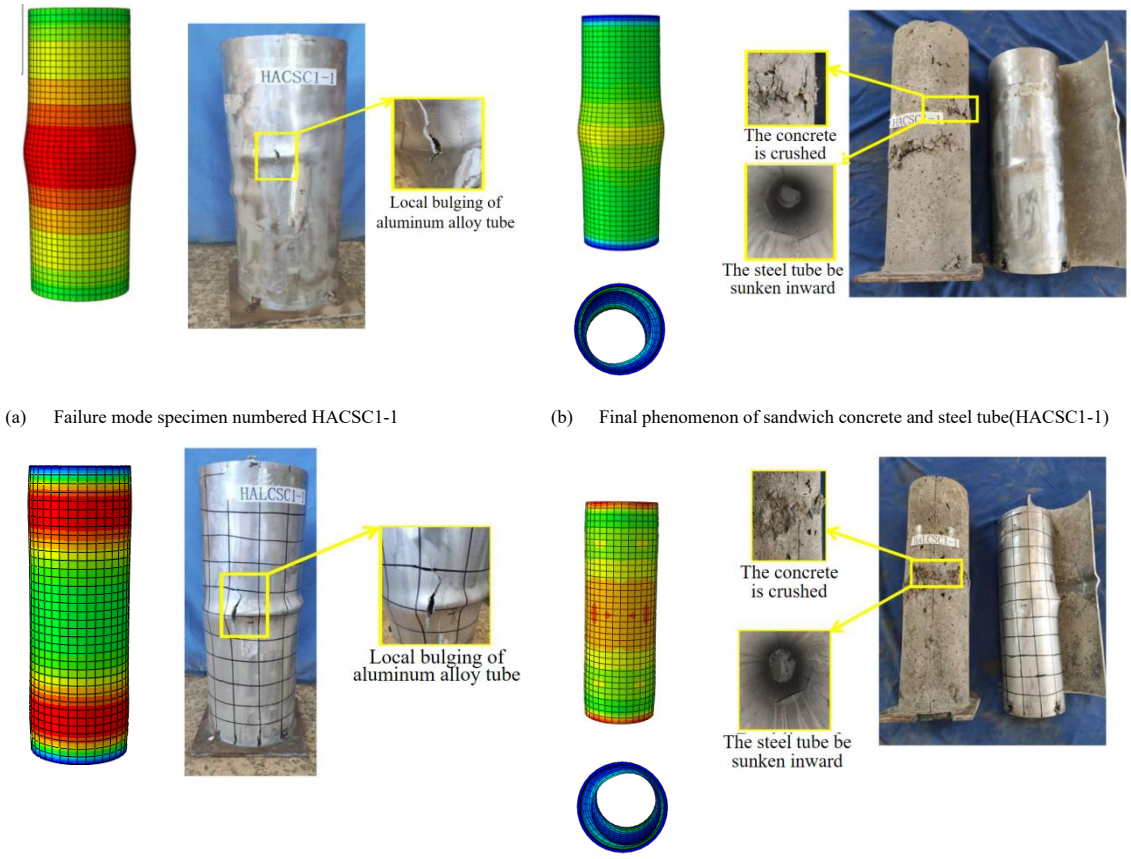

(a) Failure mode specimen numbered HACSC1-1

(b) Final phenomenon of sandwich concrete and steel tube(HACSC1-1)

(c) Failure mode specimen numbered HALCSC1-1

(d) Final phenomenon of sandwich concrete and steel tube(HALCSC1-1)

Fig. 5 Failure mode of typical specimen

3.2. Strain analysis

3.2.1. Load-strain curve

The Fig.6 illustrates the rule of longitudinal and transverse strain variations in specimens featuring ordinary and lightweight concrete as sandwich materials under axial loading. These strain measurements are derived by averaging the data collected by strain gauges AL1-L to AL4-L and AL1-T to AL4-T, which are symmetrically positioned at a height of H/2. By examining the load-strain curves depicted in figure 6 for the eight specimens, the following concise summary of the observed rules can be provided:(1) Early on in the loading process, the strain is approximately linear with the load, following the attainment of peak bearing capacity, the longitudinal and transverse strains increase rapidly, this is because when the load approaches the ultimate bearing capacity, the sandwich concrete in the middle of the column expands laterally, causing the aluminum alloy tube to be compressed by the sandwich concrete, accelerating its lateral deformation, and the lateral deformation will have a certain impact on the longitudinal strain; (2) With the decrease of the hollow ratio, the buckling longitudinal strain of the aluminum alloy tubes of the HACSC series and HALCSC series gradually increases; (3) When other conditions remain constant, the transverse deformation of the specimen using lightweight concrete as sandwich concrete is faster than the specimen using ordinary concrete, the slope of the load-strain curve is reduced, and the stiffness is smaller.

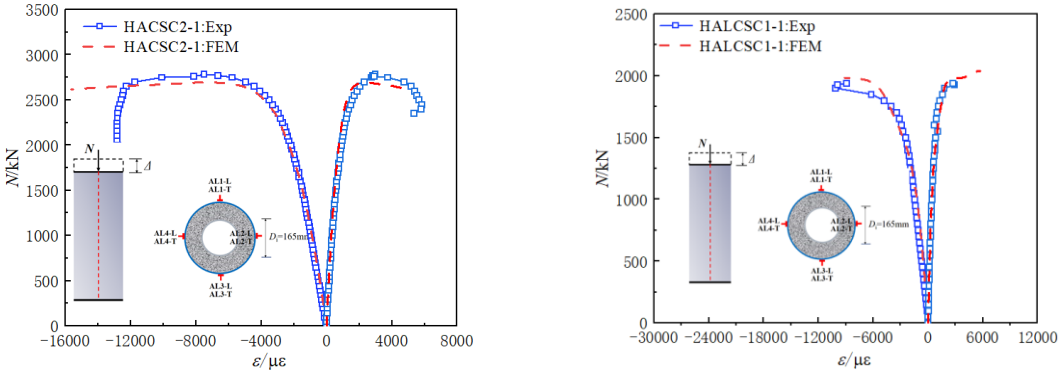

(a) HACSC1-1

(b) HALCSC1-1

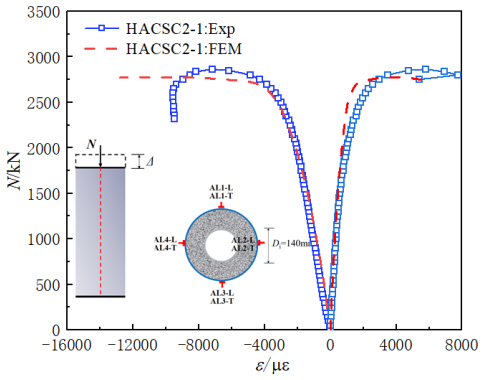

(C) HACSC2-1

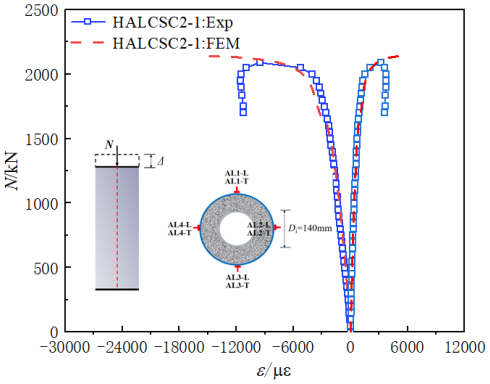

(d) HALCSC2-1

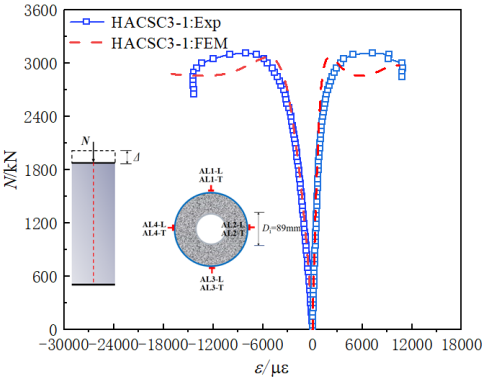

(e) HACSC3-1

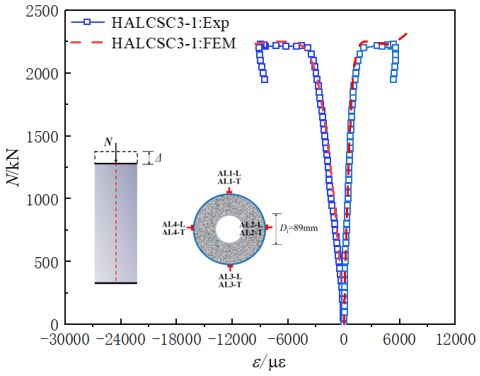

(f) HALCSC3-1

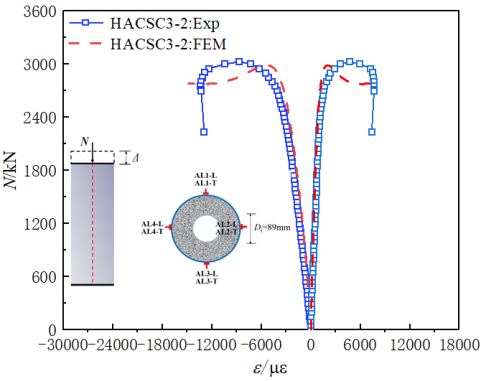

(g) HACSC3-2

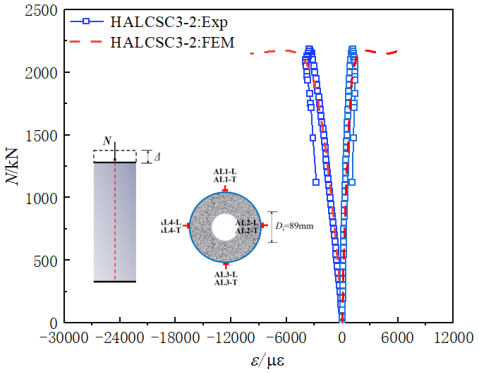

(h) HALCSC3-2

Fig. 6 Load-strain curve

3.2.2. Transverse deformation coefficient

Continuously increase the load until reaching a specific characteristic point, aluminum alloy tube has just begun to exert a progressive restraining influence on the sandwich concrete. For the further study of confinement mechanism of aluminum alloy tube on sandwich concrete at different stress stage, the transverse deformation coefficient is introduced[16-17], it is the ratio of the transverse strain (ε_{AL-T}) and the longitudinal strain(ε_{AL-L})of the aluminum alloy tube. The relationship curves of the transverse deformation coefficient ($\varepsilon_{AL\text{-}T}/\varepsilon_{AL\text{-}L}$) with the load of the HACSC series and HALCSC series specimens are exhibited in Fig. 7(a) and (b).

The diagram in Fig.7(a) illustrates that at the inception phase of loading, the transverse deformation coefficient rises and gradually converges towards the Poisson's ratio of aluminum alloy materials. During this phase, the interaction between the aluminum alloy tube and the sandwich concrete is negligible, and the entire specimen undergoes uniaxial compression. As loading progresses to later stages, the transverse deformation coefficient surpasses the intrinsic Poisson's ratio of the aluminum alloy tube and continues to climb. This is due to the progressive increase in plastic deformation of the sandwich concrete with rising loads, resulting in greater transverse deformation of the concrete at the column's center compared to the aluminum alloy tube. Upon reaching the ultimate bearing capacity, the transverse deformation coefficient decreases, which is attributed to internal buckling of the steel tube, causing the specimen's transverse deformation to develop inwardly.

When Fig.7(a) is compared with Fig.7(b), it becomes apparent that the HALCSC series specimens exhibit a lower transverse deformation coefficient compared to the HACSC series, this is because the transverse and longitudinal deformation of the specimen using lightweight concrete as sandwich concrete is faster than the specimen using ordinary concrete, however, the longitudinal strain exhibits a quicker rate of increasing than the transverse strain.

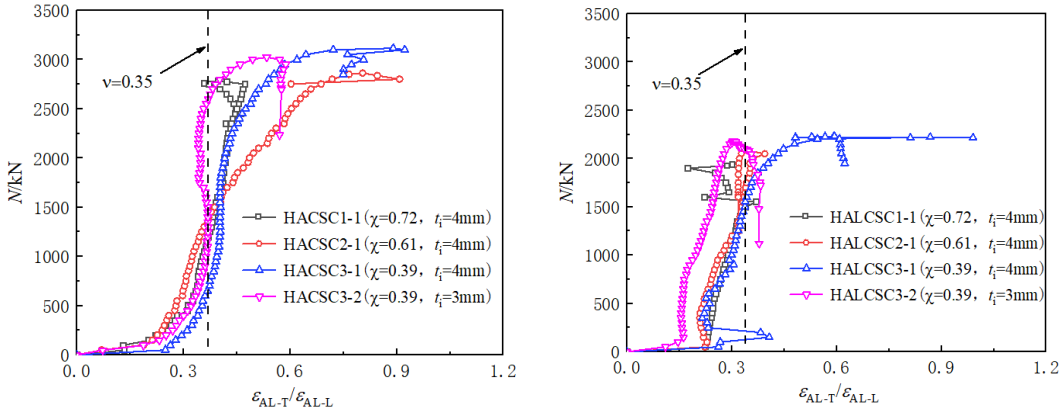

(a) HACSC series (b) HALCSC series

Fig. 7 Load- transverse deformation coefficient curve

3.3. Representative axial compression mechanical performance indicators

3.3.1. Load-displacement curve

Fig.8 displays the load-displacement profiles for specimens, while Table 1 outlines the ultimate bearing capacities derived from these profiles. The graphical representation in Fig.8 clearly indicates that eight specimens exhibit a largely similar trend in their load-displacement curves, progressing sequentially through a linear increase, a nonlinear increase, and a descent or stabilization phase. These phases are classified as the elastic stage, the elastic-plastic stage, and the plastic stage, respectively.

The rules drawn from comparing the ultimate bearing capacities of specimens across various parameters listed in Table 1 are as follows. (1) Upon decreasing the hollow ratio from 0.72 to 0.61 and further to 0.39, the HACSC series (and HALCSC series) specimens showed an increase in their ultimate bearing capacities by 3.28% and 12.38% (7.72% and 14.95%), respectively. This suggests that, while reducing the hollow ratio does enhance the bearing capacity somewhat, its impact is relatively modest when the geometric dimensions and material strength of the specimens remain unchanged. (2) When the wall thickness t_i of the steel tube was incremented from 3mm to 4mm, the ultimate bearing capacity of the HACSC series (and HALCSC series) specimens rose by 3.04% (2.09%). This is because the interaction between the steel tube and the sandwich concrete remains limited throughout the loading process, and the steel tube experiences inward local buckling during the later stages of loading. Consequently, augmenting the wall thickness of the steel tube contributes only marginally to the bearing capacity of the specimens. (3) In comparison to the HALCSC series specimens, the HACSC series specimens with hollow ratios of 0.72, 0.61, and 0.39 demonstrated significant increases in their bearing capacities by 43.4%, 37.0%, and 39.7% respectively. This is due to the superior composite strength exhibited by the aluminum alloy tube and sandwich concrete in the HACSC series specimens, which surpasses that of the HALCSC series specimens.

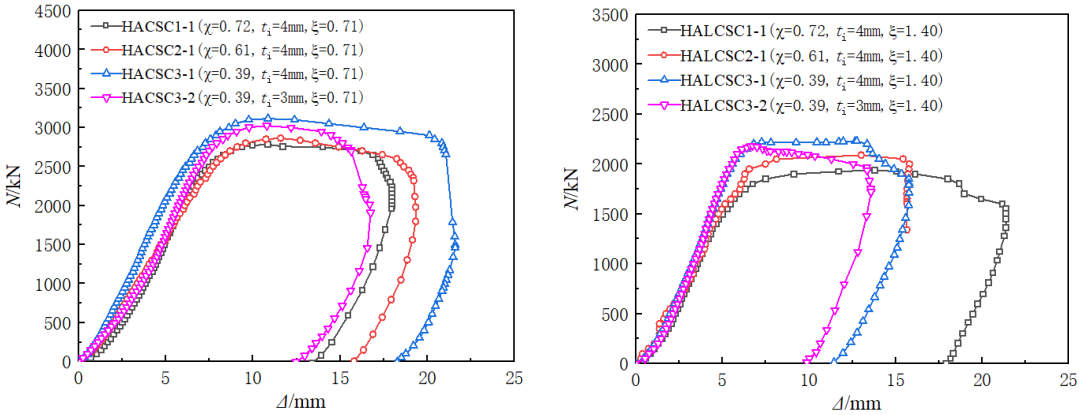

(a) HACSC series (b) HALCSC series

Fig. 8 Load-displacement curve

3.3.2. Axial compressive stiffness

Axial compression stiffness is a key indicator reflecting the ability of specimens to resist axial deformation, it can be calculated based on Ref. [18], the calculation formula can be expressed as follows:

$$EA = 0.4N_{ue} \cdot H / \Delta_{0.4} \quad (1)$$

Where EA represents the axial compression stiffness, N_{ue} is the ultimate bearing capacity, H represents the height of the column , $\Delta_{0.4}$ represents the longitudinal displacement when the bearing capacity reaches 0.4 N_{ue} .

Fig.9 illustrates the axial compressive stiffness of specimens with varying parameters, Fig. 9(a) reveals a negative correlation between the hollow ratio and the axial compressive stiffness of the specimen. Specifically, as the hollow ratio rose from 0.39 to 0.61 and then to 0.72, the axial compressive stiffness of the HACSC series decreased by 20% and 27.7%, respectively, while the HALCSC series exhibited reductions of 10.2% and 13.9%. The underlying reason for this is that, during the elastic stage, the components of the specimen undergo uniaxial compression without significant interaction among them, consequently, the axial compressive stiffness of the specimen can be approximated by summing the stiffness of its individual components, an increase in the hollow ratio leads to a reduction in the sandwich concrete's area and a corresponding increase in the internal steel tube's area. Calculations indicate that the stiffness loss due to the decreased cross-section of the sandwich concrete outweighs the stiffness gain from the expanded steel tube area. Fig.9(b) displays the axial compressive stiffness of specimens with different wall thicknesses. It is apparent from Fig.9(b) that an increment in the steel tube's wall thickness from 3 mm to 4 mm results in a 21.6% increase in the axial compressive stiffness of the HACSC series and a 4.3% increase in the HALCSC series. This occurs because augmenting the wall thickness of the steel tube expands its cross-sectional area, subsequently boosting the specimen's capacity to withstand axial deformation.

In conclusion, the axial compressive stiffness is significantly influenced by the cross-sectional area, making it imperative to thoroughly consider the cross-sectional area ratio of each component during the structural design phase to guarantee that both strength and stiffness meet the required safety standards.

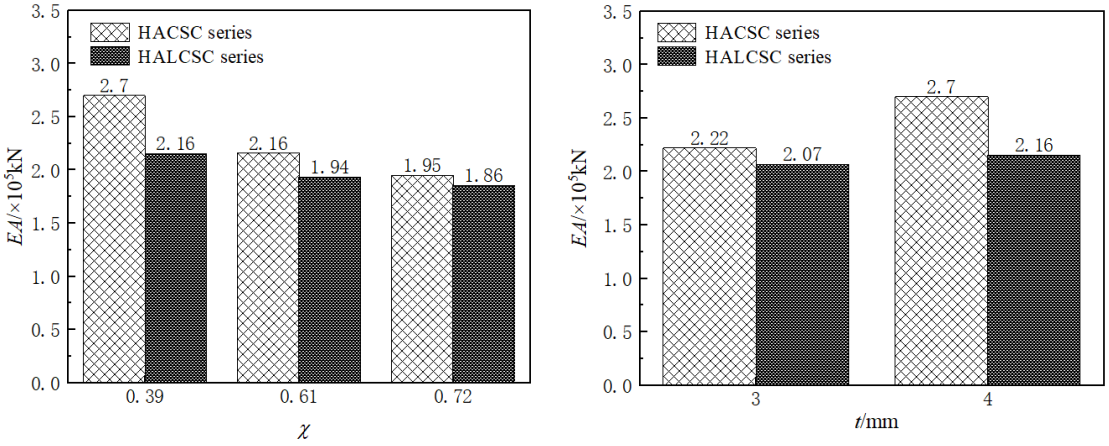

(a) Effect of hollow ratio on the axial compression stiffness

(b) Effect of the wall thickness of steel tube on the axial compressive stiffness

Fig. 9 axial compressive stiffness

3.3.3. Strength coefficient

The strength coefficient *SI* can reflect the composite effect of the specimens, the paper adopts the method recommended in Ref. [19] for calculation, the representation of SI is outlined below:

$$SI = \frac{N_{ue}}{f_{A-0.2}A_a + f_{ck}A_c + f_{yi}A_s} \tag{2}$$

Where $f_{A-0.2}$ is the nominal yield strength of the aluminum alloy tube, A_a is the area of the aluminum alloy tube's cross-section, f_{ck} is the axial compressive strength of the concrete, A_c is the area of sandwich concrete's cross-section, f_{yi} is the yield strength of the internal steel tube, A_s is the area of the internal steel tube's cross-section.

Fig.10 presents the strength coefficients *SI* of the specimens under different parameters. As illustrated in Fig.10, the *SI* of the HACSC series (HALCSC series) specimens is in the range of 1.322～1.411(1.080～1.339)，which indicates that the specimen has a good composite effect. In addition, it can also be found from Fig.10 that the *SI* of the HACSC series (HALCSC series) specimens increases by 0.38% and 5.75% (8.4% and 20.5%) when the hollow ratio decreases from 0.72 to 0.61 and 0.39 respectively, the SI increase rate of the HALCSC series specimens is faster than the HACSC series specimens, this is because the confinement effect coefficient ξ ($\xi = \alpha_n f_{A-0.2} / f_{ck}$, $\alpha_n = A_a / A_{ce}$, α_n is the nominal aluminum ratio, A_{ce} is the nominal cross-sectional area of sandwich concrete) increased from 0.71 to 1.40 when the ordinary concrete in the sandwich area is replaced by lightweight concrete, therefore, the aluminum alloy tube of the HALCSC series specimens has a stronger confinement effect on the sandwich concrete.

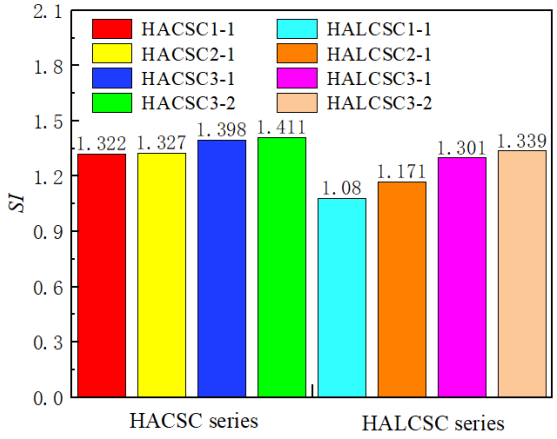

Fig. 10 the strength coefficients *SI*

4. Numerical simulation analysis

4.1. Establish finite model

4.1.1. The stress-strain relationship of each component material

4.1.1.1. Aluminum alloy

The distinctive mechanical features of aluminum alloys set them apart from steel produced through hot-rolling of low-carbon and standard low-alloy steel, as they exhibit no pronounced yield point. On that account, the stress-strain characteristics of aluminum alloys are captured using the isotropic elastoplastic constitutive model outlined in Reference [20], and this model can be mathematically expressed through Equ (3)：

$$\varepsilon_a = \frac{\sigma_a}{E_a} + 0.002\left(\frac{\sigma_a}{f_{A-0.2}}\right)^n \tag{3}$$

where σ_a and ε_a represent the stress and strain of the aluminum alloy respectively, and E_a is the modulus of elasticity of the aluminum alloy (E_a=70000MPa), n is the parameter describing strain hardening, Eq.(4) is applied to calculate it.

$$10n = f_{A-0.2}\,(MPa) \tag{4}$$

4.1.1.2. Sandwich concrete

Sandwich concrete is primarily constrained by aluminum alloy tubes, which have the difference constraining effect compared to steel tubes on concrete, therefore, the constitutive relationship of sandwich concrete adopts the equivalent compressive stress-strain model proposed in Ref. [5], which can be expressed by Eq. (4), and Fig. 11 depicts the stress-strain curve.

$$\sigma = \begin{cases} \left[\dfrac{2\varepsilon}{\varepsilon_{c0}} - \left(\dfrac{\varepsilon}{\varepsilon_{c0}}\right)^2\right] f_c^{'} & \varepsilon \le \varepsilon_{c0} \\ f_c^{'} & \varepsilon_{c0} < \varepsilon \le \varepsilon_{cc} \\ f_r + \left(f_c^{'} - f_r\right)\exp\left[-\left(\dfrac{\varepsilon - \varepsilon_{cc}}{\alpha}\right)^{1.2}\right] & \varepsilon > \varepsilon_{cc} \end{cases} \tag{5}$$

where $f_c^{'}$ represents the compressive strength of the concrete cylinder, the other indicators(f_r , ε_{co} , ε_{cc} , f_{rp} , k , α) included in equation (5) can be calculated by equation (6)~(11).

$$f_r = 0.25 f_c^{'} \tag{6}$$

$$\varepsilon_{c0} = f_c^{'} \times 10^{-5} + 0.0022 \tag{7}$$

$$\varepsilon_{cc} = \varepsilon_{c0} \times \frac{t_o}{D_o} \times \left(611k^2 - 956k + 608\right) \tag{8}$$

$$k = f_c^{'} \times \left(\frac{f_{rp}}{f_c^{'}} \right)^{0.3124+0.002 f_c^{'}} \tag{9}$$

$$f_{rp} = \frac{1+0.027 f_{A-0.2} e^{-0.02 \frac{D_o}{t_o}}}{1+1.6 e^{-10} (f_c^{'})^{4.8}} \tag{10}$$

$$\alpha = 0.04 - \frac{0.036}{1+e^{6.08\xi-3.49}} \tag{11}$$

In the Equ(6)-(11), f_r represents the compressive strength of concrete after considering strength reduction, ε_{co} denotes the strain at which peak compressive stress occurs, ε_{cc} is the strain corresponding to the confined axial compressive strength of concrete, and α stands for the strain adjustment coefficient, which is primarily related to the confinement effect coefficient.

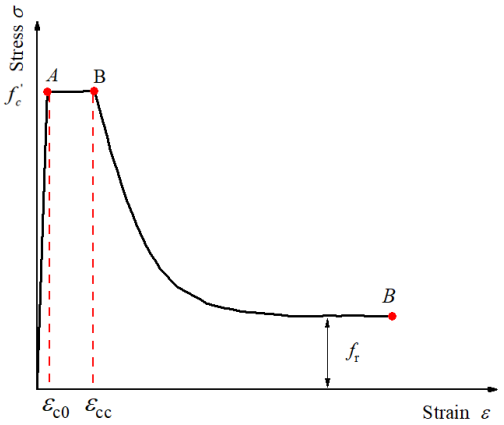

Fig.11 Stress-strain relationship curve of sandwich concrete

4.1.1.3. Steel

The constitutive model chosen for the embedded hollow steel tube is the five-stage stress-strain model introduced by Han et al. [21], and its formulation is detailed as follows.

$$\sigma_s = \begin{cases} E_s \varepsilon_s & \varepsilon_s \le \varepsilon_e \\ -A\varepsilon_s^2 + B\varepsilon_s + C & \varepsilon_e < \varepsilon_s \le \varepsilon_{el} \\ f_y & \varepsilon_{e1} < \varepsilon_s \le \varepsilon_{e2} \\ f_y \left[1+0.6 \dfrac{\varepsilon_s - \varepsilon_{e2}}{\varepsilon_{e3} - \varepsilon_{e2}} \right] & \varepsilon_{e2} < \varepsilon_s \le \varepsilon_{e3} \\ 1.6 f_y & \varepsilon_s > \varepsilon_{e3} \end{cases} \tag{12}$$

The indicators involved in formula (12) can be calculated using the following formula： $\varepsilon_e = 0.8 f_y / E_s$, $\varepsilon_{e1} = 1.5\varepsilon_e$, $\varepsilon_{e2} = 10\varepsilon_{e1}$, $\varepsilon_{e3} = 100\varepsilon_{e1}$, $A = 0.2 f_y / (\varepsilon_{e1} - \varepsilon_e)^2$, $B = 2A\varepsilon_{e1}$, $C = 0.8 f_y + A\varepsilon_e^2 - B\varepsilon_e$.

4.1.2. Element type, mesh division, constraints and boundary conditions

In Fig.12, the finite element model constructed through the use of ABAQUS is displayed, featuring a specimen that is made up of four distinct parts: the upper and lower end plates, an aluminum alloy tube, sandwich concrete, and an internal steel tube. During the process of establishing this model, 8-node solid elements (C3D8R) were utilized for modeling all four of these components.

The interface model between component surface include tangential and normal behaviors, tangential behavior adopts "hard" contact, normal behavior adopts "penalty" friction, the friction coefficient is 0.25 [9]. To avoid relative slip between the end plate and the end face of the member, “tie” is used between the end plates and the specimen end. Mesh segmentation is vital to ensuring calculation precision, the size of the mesh is 1/20 of the diameter of each component itself.

To simulate the boundary conditions under test conditions with realism, we place reference points RP1 and RP2 at the central points of the upper and lower end plates, respectively. We then couple the surfaces of these end plates to RP1 and RP2, respectively, where RP2 is constrained while an axial displacement is imposed on RP1.

Considering the initial defects caused by the fabrication and modeling assumptions of each material constituting the specimen, the initial defects will be taken as 1/1000 of the column length and defined in the finite element software in the form of low-order global buckling modes during the finite element calculation.

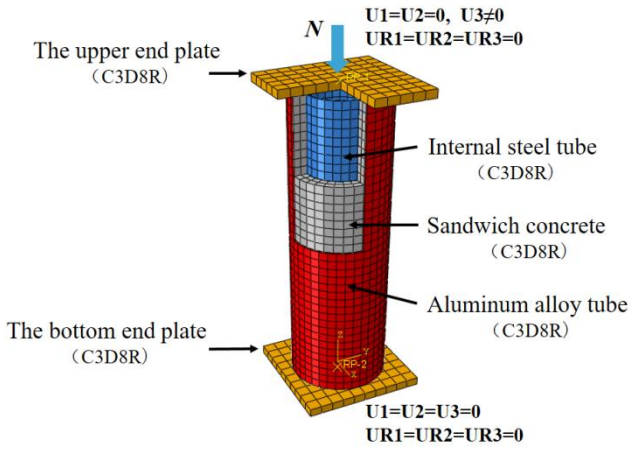

Fig.12 Schematic diagrams of model

4.2. Finite element verification

The load-strain curves of each specimen obtained through experimental and numerical simulation methods are presented in Fig.6 (a) ~ (h). Through comparison, it was found that the change trend of the load-strain curves obtained by the above two methods is basically consistent, and the ultimate bearing capacity attained through the experiment and the finite element calculation is listed in Table 1, The mean value and standard deviation $N_{u,FEM} / N_{u,e}$ are 0.99 and 0.04.

The failure mode using the experiment and finite element calculations are exhibited in Fig.5, By observing the failure modes of specimen adopting finite element calculation, it is found that the specimen was mainly manifested as bulging of the aluminum alloy tube at the middle and end of the column, the sandwich concrete at the corresponding position is crushed, and the internal steel tube was locally concave inward, which is generally consistent with the experimental phenomenon described in chapter 2.1.

In conclusion, the constitutive model and boundary conditions employed in the finite element analysis conducted in this study are dependable, enabling the finite element model to provide a more accurate assessment of the specimen's various mechanical performance indicators throughout the entire stressing process.

4.3. Analysis of working mechanism

According to the technical specification for CADST structures, a full-scale finite element model was designed as typical specimen, and the whole stressing process analysis and contact stress analysis of typical specimens were carried out. The parameter information of a typical specimen is summarized as follows: D_o=400mm, H=1200mm, D_i=195mm, ti=4mm, $\chi = 0.5$, f_{cu}=40MPa, $f_{A\text{-}0.2}$=210MPa, f_{yi}=345MPa.

4.3.1. Analysis of the whole stressing process

The figure depicted in Fig. 13 displays the load-displacement curves for a typical specimen and its constituent parts. Analyzing the trend of these curves reveals three distinct and identifiable characteristic points: Feature point A marks the yielding of the internal steel tube and the attainment of ultimate bearing capacity by the sandwich concrete; Feature point B signifies the achievement of ultimate bearing capacity by the typical specimen; and Feature point C indicates that the aluminum alloy tube has reached its ultimate bearing capacity.

The three aforementioned feature points segment the load-displacement curve into three distinct phases: the elastic phase (OA), the elastoplastic phase (AB), and the strengthening phase (BC). Figure 14 illustrates the distribution of longitudinal stresses at each of these feature points.

During the elastic stage (OA), as the displacement increases, the load rises linearly. At feature point A, the longitudinal stress within the sandwich concrete exhibits a gradual decline from the outer regions towards the center.;

Elastoplastic Stage (AB): Once the feature point A is surpassed, the load

begins to rise in a nonlinear fashion as displacement increases. When the specimen reaches feature point B, it attains its peak bearing capacity, with the loads carried by the aluminum alloy tube, sandwich concrete, and steel tube making up 31.1%, 53.5%, and 15.9% of the total axial compressive capacity of the specimen, respectively. An examination of the stress contour diagram during the elastoplastic stage reveals a gradual escalation in the average longitudinal stress of the sandwich concrete. The peak longitudinal stress, which occurs on the inner surface of the aluminum alloy tube at feature point A, amounts to 1.74 times the axial compressive strength of the concrete (1.74fck). This is owing to the aluminum alloy tube providing the utmost restraint to the sandwich concrete in this particular area.

Strengthening stage (BC): After the feature point B is exceeded, the bearing capacity of the specimen gradually decreases, sandwich concrete is constrained by aluminum alloy tubes, so its longitudinal stress variation is small; Upon attaining feature point C, the maximum longitudinal stress of the sandwich concrete is 1.76 times of the axial compressive strength, and the load-bearing capacity of the sandwich concrete reaches its peak.

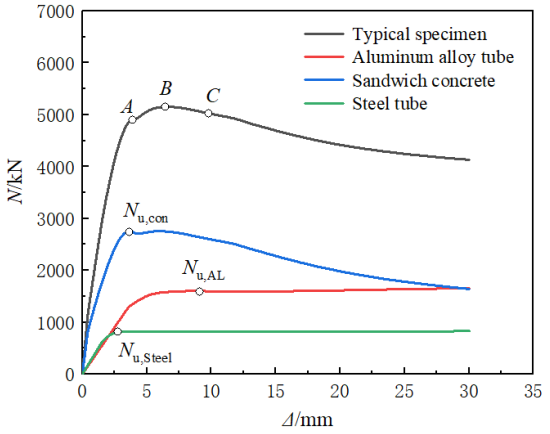

Fig. 13 Load-displacement curves of typical specimen and its components

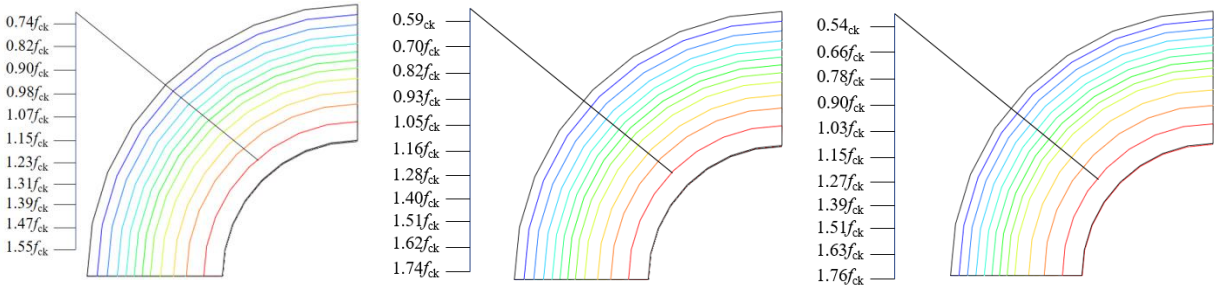

(a) feature point A (b) feature point B (c) feature point C

Fig. 14 Longitudinal stress distribution of sandwich concrete at each feature point

4.3.2. Contact stress analysis

The contact stress-displacement curves of each component at different height cross-sections of the typical specimen are shown in the Fig.15, $P1$ represents the contact stress between aluminum alloy tube and sandwich concrete, and $P2$ represents the contact stress between steel tube and sandwich concrete. As shown in the Fig.15, the contact stress between the steel tube and the sandwich concrete is always small throughout the whole stressing process, so its contact stress can be ignored, which illustrates that the internal steel tube work independently under axial compression; The contact stress value of aluminum alloy tube and sandwich concrete in the elastic stage at different height cross-sections is 0 ($P1$=0), and each part of the specimen is in a uniaxial compression state, after exceeding the feature point A, the interaction between the aluminum alloy tube and the sandwich concrete is gradually obvious, and the contact stress between the two increases, when the load of the typical specimen reaches the ultimate bearing capacity(At feature point B), the average value of the contact stresses $P1_{H/4}$ and $P1_{H/2}$ of aluminum alloy tube and sandwich concrete are0.77MPa and 0.99MPa respectively, the contact stress distribution is shown in Fig.16 ; After the feature point B is exceeded, the contact stress $P1_{H/4}$ and $P1_{H/2}$ still continue to increase.

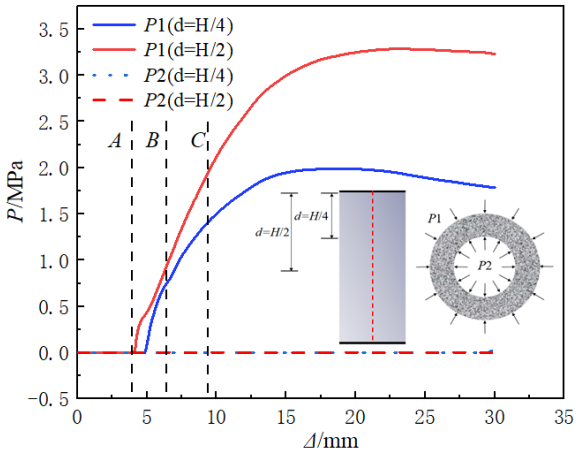

Fig. 15 The contact stress-displacement curves of each component

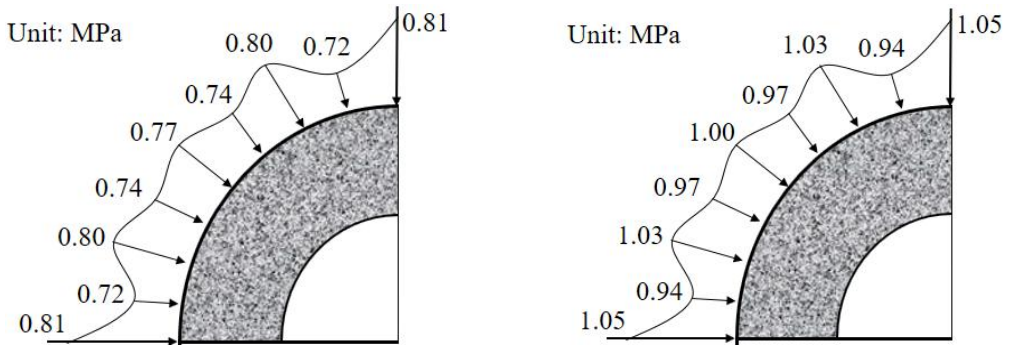

(a) cross-section at d=H/4 (b) cross-section at d=H/2

Fig. 16 Cross-section contact stress distribution at different heights under peak loads

5. Parametric analysis

Due to the limitations of current experimental conditions and the number of specimens, a lot of parameters cannot be fully covered, for the purpose of exploring the law of influence of parameters on the relevant performance of specimens， based on the typical specimens mentioned in chapter 3.3, the effects of nominal aluminum ratio, hollow ratio, concrete cube compressive strength and internal steel tube yield strength on the bearing capacity, axial compressive stiffness and ductility of specimens were subjected to detailed analysis.

5.1. Nominal aluminum ratio

When the wall thickness of the aluminum alloy tube is 3mm, 5mm, 7mm and 9mm, the nominal aluminum ratio of the corresponding specimen is 3.1%, 5.2%, 7.4% and 9.6% respectively. The effects of nominal aluminum ratio on the bearing capacity, axial compressive stiffness and ductility of the specimen are shown in Fig.17. When the aluminum ratio α_n increased from 3.1% to 5.2%, 7.4% and 9.6%, the bearing capacity of the specimen increased by 14.8%, 28.9% and 43.4%, there is no significant change in axial compressive stiffness, the ductility μ increased by 59.7%, 124.2% and 174.5%, this is because the constraint effect coefficient ξ increases from 0.24 to 0.41, 0.58 and 0.76 when the nominal aluminum ratio α_n increases from 3.1% to 5.2%, 7.4% and 9.6%, the aluminum alloy tube exerts a greater restraining effect on the sandwich concrete, causing an elevation in its strength. Furthermore, as the nominal aluminum ratio increases, the cross-sectional area of the aluminum alloy tube also increases, thereby improving the specimen's ductility.

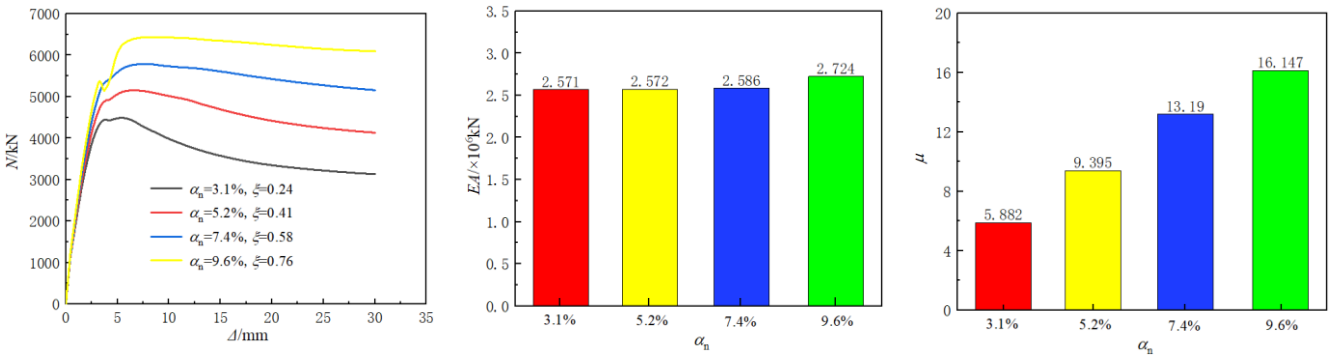

(a) Load-displacement curve (b) Axial compression stiffness (c) Ductility coefficient

Fig. 17 The influence of nominal aluminum ratio on axial compression performance indicators

5.2. Hollow ratio

By adjusting the diameter of the internal steel tube, we can achieve variations in the hollow ratio of the specimens. Specifically, when the internal steel tube's diameter is set to 0mm, 117mm, 195mm, and 273mm, the corresponding hollow ratios of the specimens are 0, 0.3, 0.5, and 0.7, respectively. Fig.18 illustrates the impacts of these hollow ratios on the specimens' bearing capacity, axial compressive stiffness, and ductility. As depicted in Fig.18, as the hollow ratio increases from 0 to 0.3, 0.5, and 0.7, the ultimate bearing capacity of the specimens decreases by 9.4%, 13.8%, and 21.8%, respectively, while the axial compressive stiffness decreases by 6.5%, 8.4%, and 20.2%. Conversely, the ductility increases by 32.9%, 40.3%, and 97.1%, respectively. This is attributed to the reduction in the sandwich concrete's cross-sectional area as the hollow ratio increases, which subsequently decreases the bearing capacity and axial compressive stiffness. Simultaneously as well, the increase in the hollow ratio enlarges the cross-sectional area of the internal steel tube, leading to an increase in the specimen's steel ratio and ultimately enhancing its ductility.

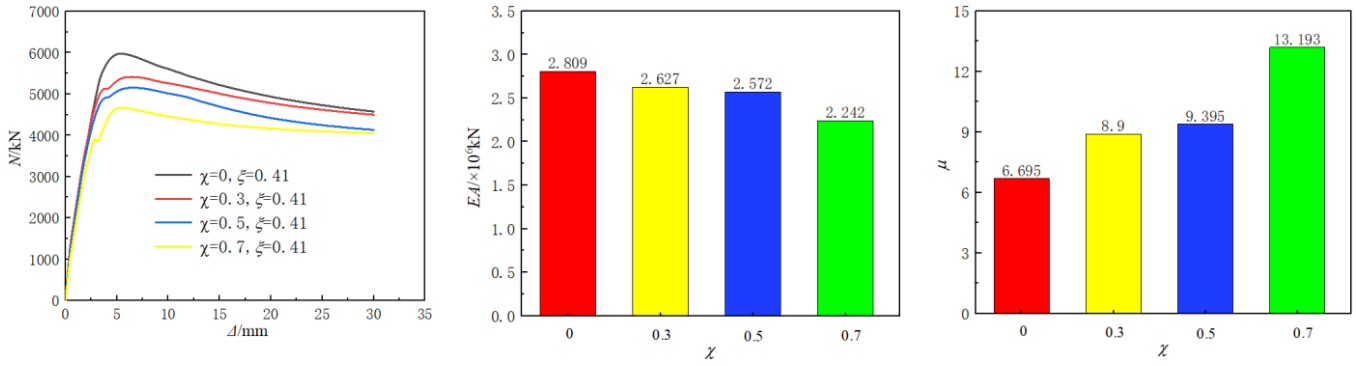

(a) Load-displacement curve (b) Axial compression stiffness (c) Ductility coefficient

Fig. 18 The influence of hollow ratio on axial compression performance indicators

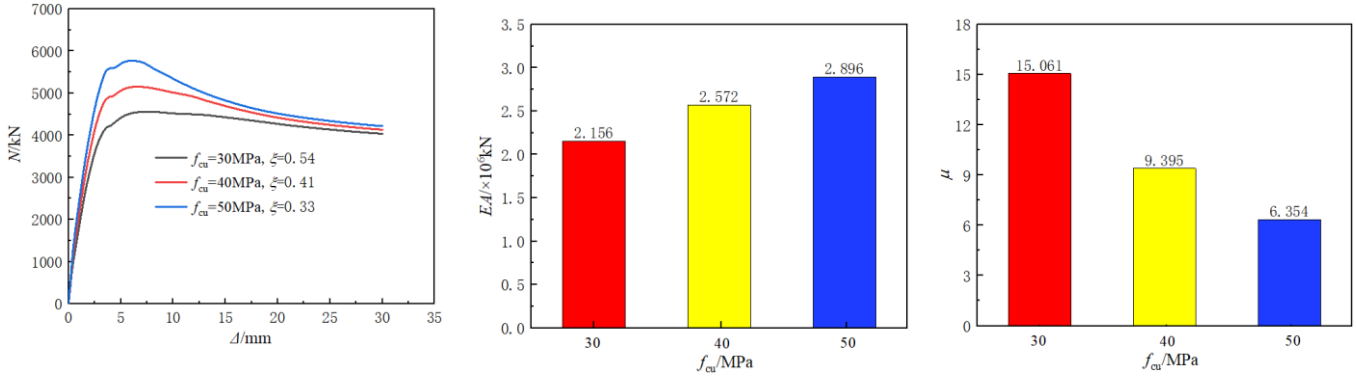

(a) Load-displacement curve (b) Axial compression stiffness (c) Ductility coefficient

Fig. 19 The influence of concrete cube compressive strength on axial compression performance indicators

5.3. Concrete cube compressive strength

The graphical representation in Fig.19 illustrates how the compressive strength of concrete cubes influences the specimen's load-bearing capacity, stiffness in axial compression, and ductility. According to Fig.19, as the concrete cube compressive strength f_{cu} rose from 30MPa to 40MPa and then to 50MPa, the ultimate load-bearing capacity augmented by 12.9% and 26.5% respectively. Similarly, the stiffness in axial compression increased by 19.3% and 34.3%. Conversely, the ductility coefficient decreased by 37.6% and 57.8% respectively. This is because, with the cross-sectional area of the components remaining constant, an elevation in the compressive strength of the concrete cubes results in an increase in load-bearing capacity. Furthermore, an increase in the compressive strength of the concrete cubes leads to a corresponding rise in the concrete's elastic modulus, thereby directly enhancing its stiffness in axial compression. However, the higher the compressive strength of the concrete, the more pronounced its brittle nature becomes, causing a gradual decrease in the specimen's ductility.

5.4. Internal steel tube yield strength

Fig.20 demonstrates the influence of the yield strength of the internal steel tube on the specimen's bearing capacity, axial compressive stiffness, and ductility. According to the data presented in Fig.20, as the yield strength of the internal steel tube rose from 235MPa to 345MPa and subsequently to 420MPa, the ultimate bearing capacity increased by 5.3% and 9.0%, respectively. Similarly, the axial compressive stiffness augmented by 2.7% and 4.2%, and the ductility coefficient also rose by 5.6% and 6.7%. The aforementioned research findings reveal that the yield strength of the internal steel tube exerts a relatively minor influence on the bearing capacity, axial compressive stiffness, and ductility coefficient. This is attributed to the lack of substantial interaction between the internal steel tube and the sandwich concrete during axial compression, as well as the occurrence of concave buckling in the steel tube during the later stages of loading. Consequently, enhancing the yield strength of the internal steel tube contributes less significantly to improving the bearing capacity, axial compressive stiffness, and ductility.

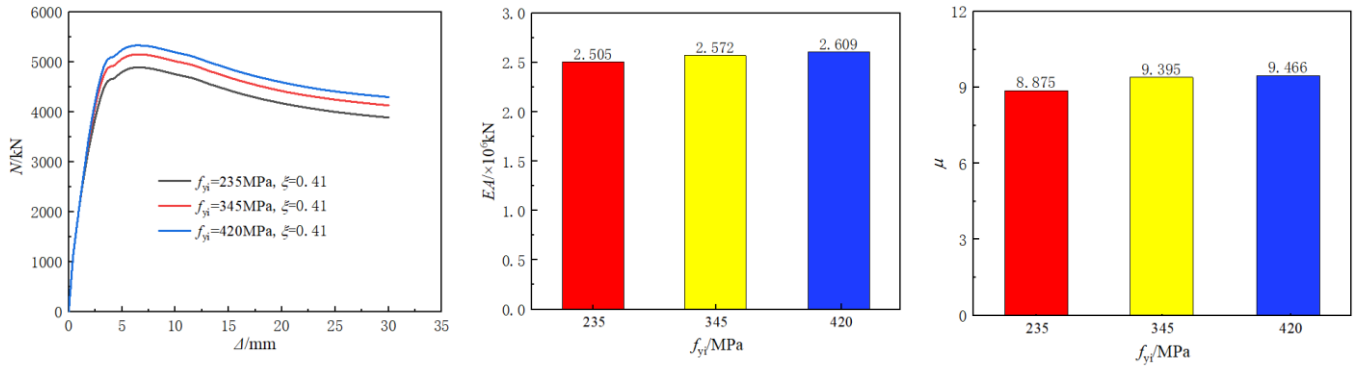

(a) Load-displacement curve (b) Axial compression stiffness (c) Ductility coefficient

Fig. 20 The influence of internal steel tube yield strength on axial compression performance indicators

6. Practical bearing capacity calculation method

Drawing upon the insights from section 3.3.2, it is possible to conclude that there is insignificant interaction between the internal steel tube and the sandwich concrete. Therefore, the bearing capacity of the specimen can be approximated by summing the bearing capacity contributed by the aluminum alloy tube and sandwich concrete composite action, and the bearing capacity provided by the internal steel tube. Guided by the superposition principle outlined in the Technical Specification for CFDST Structures (T/CCES7-2020) [22], we propose an equation to determine the axial compressive load-bearing capacity of concrete filled circular aluminum alloy tubular column with built-in hollow steel tube.

$$N_{u,acs} = N_{u,ac} + N_{is}$$

$$N_{u,ac} = f_{oac} \cdot (A_a + A_c)$$

$$N_{is} = f_{yi} A_s$$

Where $N_{u,acs}$ is the bearing capacity of CFAT column with built-in hollow steel tube, $N_{u,ac}$ represents the bearing capacity of the aluminum alloy tube and sandwich concrete composite action, $N_{u,is}$ represents the bearing capacity of the internal steel tube, f_{oac} is design values for the composite strength of aluminum alloy tube and sandwich concrete.

Considering that the CFAT column with built-in hollow steel tube is a structural design refined from the CFAT column, therefore ,it is necessary to first assess the composite axial compressive strength f'_{oac} of CFAT column, then calculating the design value of the composite strength of aluminum alloy tube and sandwich concrete f_{oac} . References [5,23-24] conducted experimental analysis and theoretical research on CFAT column under different parameters, the relationship between the confinement effect coefficient ξ and f'_{oac} / f_{ck} was obtained by collecting and processing relevant data, through Origin fitting, it was found that there is a good linear relationship between ξ and f'_{oac} / f_{ck} , the correlation between the composite axial compressive strength f'_{oac} of CFAT column and the confinement effect coefficient ξ is expressed as follows:

$$f'_{oac} = (1.1967\xi + 1.3631) f_{ck}$$

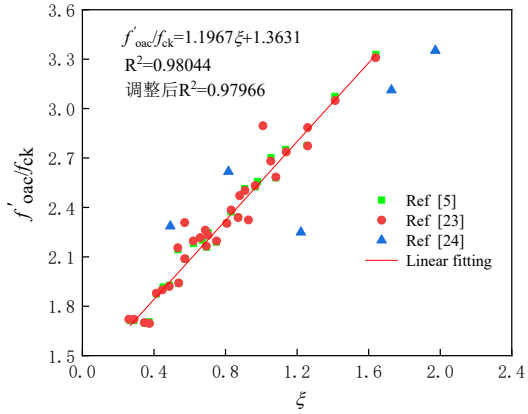

Fig.21 The relationship of f'_{oac} / f_{ck} - ξ

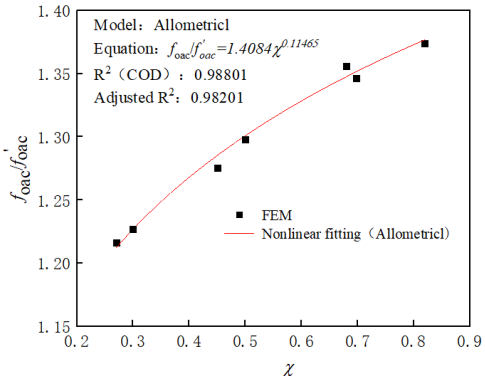

Fig. 22 f_{oac} / f'_{oac} and χ fitting results

Furthermore, taking a typical specimen as an example to study the correlation between hollow ratio χ and f_{oac}/f'_{oac}, the hollow ratio χ is taken as 0.27, 0.3, 0.45, 0.5, 0.68, 0.7, and 0.82 respectively, the correlation between hollow ratio χ and f_{oac}/f'_{oac} of the specimen was obtained by nonlinear fitting as follows:

$$f_{oac}/f'_{oac}=1.4084\chi^{0.11465}$$

To summarize, the load-bearing capacity $N_{u,ac}$ of the aluminum alloy tube and sandwich concrete, when subjected to composite action, can be formulated as outlined below.

$$N_{u,ac}=1.4084\chi^{0.11465}\left(1.1967\xi+1.3631\right)f_{ck}(A_a+A_c)$$

Utilizing the superposition principle, the equation for assessing the load-bearing capacity of a circular aluminum alloy tube column filled with concrete and featuring an integral hollow steel tube is presented below:

$$N_{u,acs}=1.4084\chi^{0.11465}\left(1.1967\xi+1.3631\right)f_{ck}(A_a+A_c)+f_{yi}A_s$$

The bearing capacity $N^{c}_{u,acs}$ of 8 specimens was calculated using the proposed bearing capacity formula, and compared with the test measured and finite element simulation results $N^{t+FEM}_{u,acs}$, The comparison results are shown in Fig.23, between the above two have a deviation of 9.9% to -19.4%, this indicates that the proposed bearing capacity calculation formula can effectively predict the axial compressive bearing capacity of CFAT column with built-in hollow steel tube.

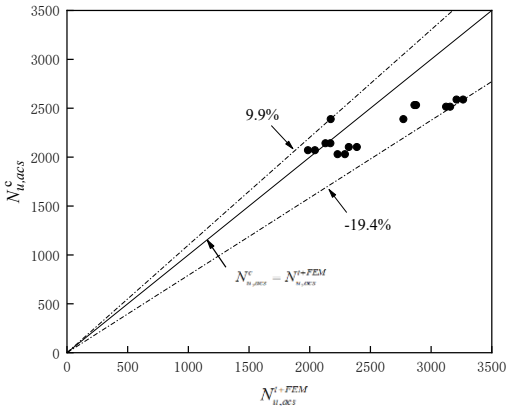

Fig. 23 Comparison between calculation results and test (finite element) results

7. Conclusions

Through experiments and numerical simulations, a thorough and systematic evaluation has been conducted on the performance indicators of the innovative component presented in this paper. Drawing from current research findings, the conclusions can be derived are listed as follows.

The failure mode of CFAT column with built-in hollow steel tube under axial compression is manifested as local bulging at the middle or top of the column, aluminum alloy tube exhibit local bulging and even cracking, the concrete located at the corresponding area has been fractured, and the internal steel tube presents concave buckling, each component demonstrates good deformation coordination.

The type of concrete is pivotal in determining both the load-bearing capacity and stiffness of the specimens. When the hollow ratio is 0.72, 0.61, and 0.39, the bearing capacity of specimens with ordinary concrete as the sandwich concrete is 43.4%, 37.0%, 39.7% larger than specimens with lightweight concrete as the sandwich concrete, and the axial compression stiffness is 4.8%, 11.3%, and 25% greater than them. Increasing the wall thickness of the internal steel tube has a relatively small impact on the bearing capacity and stiffness of the specimen. Through calculation, it was found that the strength coefficients *SI* of two types of specimens (HACSC series and HALCSC series) were greater than 1, which indicate a good composite effect between the components

Through numerical simulation analysis methods, the working mechanism of the specimen was studied, including the analysis of the entire stress process and contact stress. The study found that most of the load was shared by the sandwich concrete during the entire stress process, and The failure sequence of the specimen unfolds as follows: The yield of internal steel tube and the ultimate bearing capacity of sandwich concrete almost occur simultaneously→ the load of the specimen reaches its ultimate bearing capacity→ aluminum alloy tube reach their ultimate bearing capacity. Meanwhile, the findings from the contact stress analysis demonstrate a nearly absent level of interaction at the interface between the inner steel tube and the sandwich concrete.

The results of parameter analysis reveal that the aluminum ratio exerts the most prominent influence on the specimen's load-bearing capacity and ductility. Specifically, as the aluminum ratio escalated from 3.1% to 5.2%, 7.4%, and 9.6%, the specimen's load-bearing capacity augmented by 14.8%, 28.9%, and 43.4%, respectively, while its ductility coefficient soared by 59.7%, 124.2%, and 174.5%. Conversely, fluctuations in the yield strength of the internal steel tube had a comparatively minor effect on the specimen's load-bearing capacity, axial compression stiffness, and ductility.

Following a comparison of the results derived from the formula calculation, rooted in pertinent technical specifications and parameter evaluations, with the experimental (finite element modeling) data for concrete filled circular aluminum alloy tubular column with built-in hollow steel tube, it was evident that the proposed method for calculating bearing capacity exhibited good practical utility, with deviations within a range of -19.4% to 9.9%.

Reference

[1] L.H. Han, Y.F. Yang, Technology of concrete with tubular structures. Beijing: China Architecture & Building Press, 2004.
[2] X.H. Zhou, Y.H. Wang, G.B. Lu, et al. Mechanical behavior of concrete filled double skin steel tubular columns under cyclic pure torsion. Journal of Building Structures 38. S1(2017):266-271.
[3] H.Y. Xu, Z.W. Yu. Behavior analysis of concrete-filled double skin steel tubular columns under axial loading. Journal of Huazhong University of Science and Technology (Natural Science Edition), 39.12(2011):123-127.
[4] Z.B. Wang, H.Y. Gao, S. Y. Chi, et al. Behavior of concrete-filled double-skin thin-walled steel tubular columns under eccentric compression. Journal of Building Structures (2018).
[5] X. Zeng, W.B. Wu, J.S. Huo, et al. The axial strength of concrete-filled aluminum alloy circular tubular stub columns. Engineering Mechanics, 38.2(2021):52-60.
[6] X.Y. Li, G.H. Xing, P.Y. Zhang, et al. Calculation on bearing capacity of 7075 high-strength aluminum alloy tubular confined concrete column under axial compression. Industrial Construction, 50.11(2020):162-167.
[7] D. Chen, H. Qu, W. Li, et.al. Mechanical Property of Seawater Sea-sand Concrete-filled Aluminum Alloy Circular Tubular Columns under Axial Load. Journal of Yantai University (Natural Science and Engineering Edition), 35.04(2022):467-475.
[8] Y. Shi, J.G. Zhang, T. Wang, et al. Experimental study on the axial compression performance of a new type of metal tube concrete short column. Building Structure, 52.03(2022):110-115.
[9] F. Zhou, B. Young. Concrete-filled double-skin aluminum circular hollow section stub columns. Thin-Walled Structures 133.12(2018):141-152.
[10] X.X. Zha, Y.L. Gong. Behavior study of new type concrete filled metal tubular (CFMT) I: Columns strength capacity of axially compressed short columns. Progress in Steel Building Structures, 14.03(2012):12-18+35.
[11] F. Zhou, B. Young. Numerical analysis and design of concrete-filled aluminum circular hollow section columns. Thin-Walled Structures, 50.1(2012):45-55.
[12] F.C. Wang, H.Y. Zhao, L.H. Han. Analytical behavior of concrete-filled aluminum tubular stub columns under axial compression. Proceedings of the 12th International Conference on Advances in Steel-Concrete Composite Structures. ASCCS 2018.
[13] Patel V I, Liang Q Q, Hadi M N S. Numerical simulations of circular high strength concrete-filled aluminum tubular short columns incorporating new concrete confinement model. Thin-Walled Structures 147.
[14] GB/T 228.1. Metallic materials-tensile testing-part 1: method of test at room temperature. Standards Press of China, Beijing, 2010.
[15] Standard for test methods of concrete physical and mechanical properties: GB/T 50081-2019. Beijing: China Architecture & Building Press, 2019.
[16] F. X. Ding, Z. Li, S. S. Cheng, et al. Composite action of hexagonal concrete-filled steel tubular stub columns under axial loading. Thin Walled Structures 107(2016):502-513.
[17] Q. Rong, Y.S. Zeng, X.M. Hou, et al. Experimental study on mechanical behavior of RPC-filled circular steel tube columns under axial compression. Journal of Building Structures (2019).
[18] H. Zhao, Y. Zhang, R Wang. Study on mechanical behavior of square hollow concrete-encased CFST columns with inner steel plate under axial compression. Journal of Building Structures, 43.06(2022):53-62+141.
[19] Li Y J, Han L H, Xu W, et al. Circular concrete encased concrete-filled steel tube (CFST) stub columns subjected to axial compression. Magazine of Concrete Research 68.19(2016):995-1010.
[20] Ramberg W, Osgood W R. Description of stress-strain curve by three parameters [R]. Washington DC, USA: National Advisory Committee for Aeronautics, 1943.
[21] Han L H, An Y F. Performance of concrete-encased CFST stub columns under axial compression. Journal of constructional steel research. 93.7(2014):62–76.
[22] Chinese Code, Technical specification for concrete-filled double skin steel tubular structures: T/CCES 7-2020, Beijing, China, 2020.
[23] T Hu . Study on concentric compressive behavior of concrete-filled Aluminum Alloy Circular Tubular Stub Columns. Hainan University, 2019.
[24] Y Q LIU. Experimental study on axial compression of concrete stub column with round Aluminium alloy tube . Shenyang Jianzhu University,2020 .